

Frequency-Domain Optical Metrology Data Fusion

by

George Andrew Smith

Copyright © George Andrew Smith 2022

A Masters Report Submitted to the Faculty of the

JAMES C. WYANT COLLEGE OF OPTICAL SCIENCES

In Partial Fulfillment of the Requirements

For the Degree of

MASTER OF SCIENCE

In the Graduate College

THE UNIVERSITY OF ARIZONA

2022


THE UNIVERSITY OF ARIZONA
GRADUATE COLLEGE

As members of the Master's Committee, we certify that we have read the thesis prepared by George Andrew Smith, titled: Frequency-Domain Optical Metrology Data Fusion and recommend that it be accepted as fulfilling the dissertation requirement for the Master's Degree.



Daewook Kim

Date: May 9, 2022



Heejoo Choi

Date: May 9, 2022



Michael Hart

Date: May 9, 2022

Final approval and acceptance of this thesis is contingent upon the candidate's submission of the final copies of the thesis to the Graduate College.

I hereby certify that I have read this thesis prepared under my direction and recommend that it be accepted as fulfilling the Master's requirement.



Daewook Kim

Date: May 9, 2022

Master's Thesis Committee Chair
College of Optical Sciences

ARIZONA

Acknowledgements

I want to thank Dr. Michael Hart and Dr. Johanan Codona at HartSci for working with the UA team throughout the duration of this project. A special thanks to Dr. Daewook Kim and Dr. Heejoo Choi for their exceptional guidance and support.

Hyukmo Kang, Kevin Derby, Henry Quach, and Jaren Ashcraft
My friends and lab mates, thank you for making my day-to-day time in lab more enjoyable,
and my time as a graduate student at the U of A more memorable.

Table of Contents

Abstract.....	5
Chapter 1. Introduction	6
Chapter 2. Metrology Principle.....	8
2.1 Deflectometry	9
2.2 Interferometry	14
Chapter 3. Data Collection Process and System Calibration	18
3.1 Deflectometry Calibration	20
3.2 Motorized Translation Stage Calibration.....	21
Chapter 4. Data Analysis and Metrology Data Merging	22
4.1 Polynomial Fitting and Merging.....	22
4.2 Frequency Domain Merging	24
4.3 Low and High-Pass Filter Masks	27
4.4 Mask Application Adjustability	36
4.5 Verification Through Synthetic Data Evaluation.....	38
Chapter 5. Conclusions and Future Work.....	40
Chapter 6. References	41

Abstract

Currently X-ray source technologies are advancing at a rate that X-ray optics cannot keep up with. The challenge now is to advance the X-ray optics fabrication techniques so that they can appropriately focus, monochromate, and manipulate these beams. Advancements in optical fabrication for these mirrors require commensurate advancements in the metrology techniques used for guiding the deterministic computer-controlled fabrication process. In order to meet the extreme surface shape and surface roughness requirements for these extreme applications, we suggest a metrology data process that merges two different maps of the same surface together. In this paper we introduce a methodology for merging together data sets of different spatial resolutions and fields of view without distorting the original profile. Through application of various frequency-domain merging masks, we demonstrate the versatility and potential for this methodology to be applied in the various fabrication processes for extreme optical surfaces that require high accuracy across all spatial frequency domains.

Chapter 1. Introduction

As advancements in X-ray sources continues there is a commensurate need to advance the quality of optics that shape and transport the beam. Currently our ability to utilize these advancements in X-ray source technology are limited by our inability to fabricate these specialized high-quality optics. Many of the unique opportunities viable through diffraction limited X-ray sources – such as single-molecule coherent X-ray imaging, nanodiffraction, nanoprobe spectroscopy, etc. – demand maximum intensity at focus and are extremely sensitive to wavefront distortion [1]. Consequently, these applications require mirrors with ≤ 0.5 -nm rms (root mean square) figure height errors, and < 0.1 -nm rms surface roughness errors over clear apertures on the scale of $\sim 10 \times 100$ mm. These error specifications are the current gold standard for short, flat, or low-curvature mirrors. These fabrication capabilities must be expanded to 1-m class mirrors with high radii of curvature in order to meet the pioneering work in X-ray sciences. It is therefore essential to develop metrology tools applicable for high resolution measurements over large areas.

For meaningful progress to be made in the fabrication of these high-perfection mirrors, vendors require metrology tools capable of rapid, highly accurate surface characterization for iterative surface figure refinement. For the case of 1-meter class mirrors, desirable measurement times are less than an hour [1]. In order to meet the necessary metrology capabilities for surface height and roughness precision for large testing areas, we suggest a method for combining interferometric and deflectometric measurements made over sub-apertures. The basis for these two optical metrology techniques being selected is the high accuracy surface figure data achieved through deflectometry, the high accuracy surface roughness data achieved through microscopic

white light interferometry, and the capability for these two metrology techniques to effectively compensate for each other's limitations.

Chapter 2. Metrology Principle

This hybrid metrology technique starts with two sets of measurements being taken, one set comprised of many stitched White Light Interferometry (WLI) sub-apertures, and one set comprised of a singular full aperture measurement through deflectometry. The interferometric sub-apertures are stitched together using the stitching functionality available through the WLI, with the overlapping region between sub-apertures impacting the acquisition time and the low shape error as shown in Figure 1.

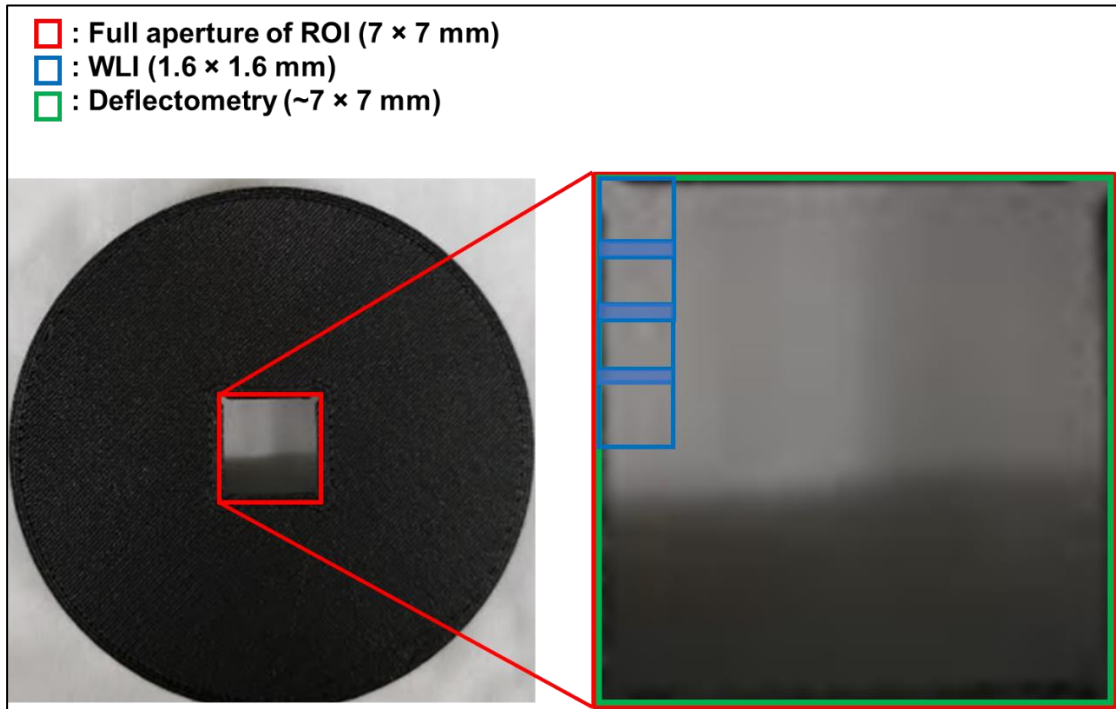


Figure 1. Illustration of deflectometry aperture sizes ($\sim 7 \times 7$ mm) in comparison to White Light Interferometer (WLI) sub-aperture sizes (1.6×1.6 mm) across a full 7×7 mm ROI (Region of Interest). Shaded areas represent overlap regions between WLI sub-apertures. Larger overlap regions lead to less low shape error after the stitching process at the cost of increased data acquisition time.

Through the completion of the WLI sub-aperture stitching process two maps of the same surface are obtained, one taken through interferometry, and one taken through

deflectometry. During this stitching process uncertainty in the low-order surface shape of the interferometric data becomes an issue due to both the size of the overlapping sub-aperture regions and the number of sub-apertures that must be stitched to measure the entirety of the surface [2]. The issue of unreliability in the overall low-order surface shape information for the stitched interferometric surface map is compensated for by using the low-order deflectometry data (after calibration) as a reliable framework to place the accurate higher order interferometric data on to. By “fusing” these two metrology techniques in the frequency domain together, high accuracy data is used for both the lower and higher order surface structure, while minimizing the overlap region size required for the sub-apertures. This is essential to maintaining the integrity of the surface data while reducing the time to measure the entirety of the optical surface.

2.1 Deflectometry

Deflectometry is an incoherent optical metrology technique that uses the law of specular reflection and geometrical location information to determine the local surface slope of a test surface, or unit under test (UUT). Illustrated in Figure 2. [5], there are three main components to any basic deflectometry system; an LCD screen used to display fringe patterns, a UUT that reflects the light from the display, and a camera that is focused on the UUT that detects the light that is reflected off the UUT’s surface. The camera is focused onto the UUT’s surface in order to establish conjugate imaging with the UUT being illuminated by the fringe pattern from the LCD display.

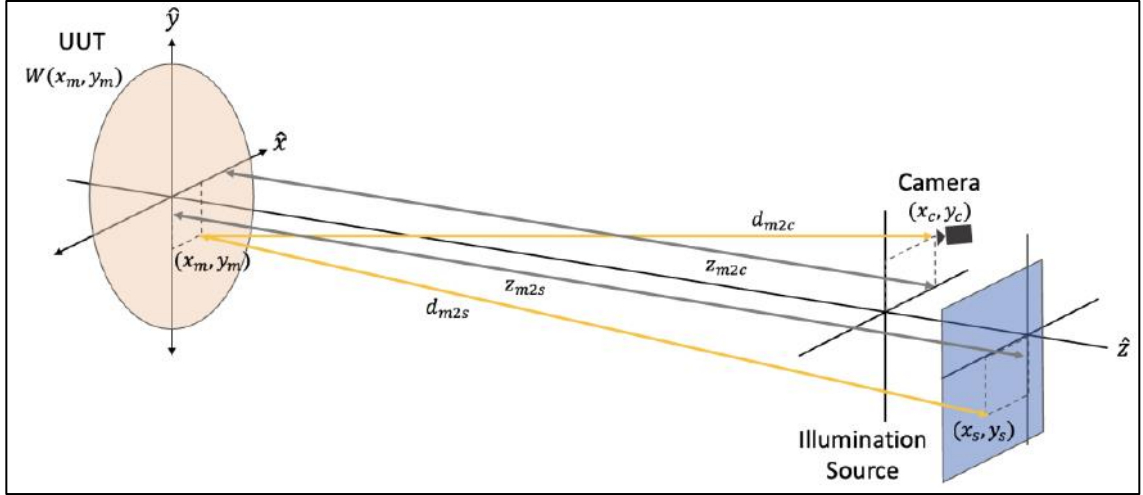


Figure 2. Classical setup for deflectometry comprised of a camera, UUT, and light source (figure from Henry Quach et al. [5]).

Through knowledge of each component's 3-dimensional locations and dimensions relative to one another, the law of specular reflection can be used to trace individual points of illumination from the source to the camera. The \hat{z} axis defines the optical axis of the UUT and the deflectometry system, the \hat{y} and \hat{x} axes determine the direction of the tangential and sagittal planes, respectively. The coordinates (x_m, y_m) , (x_s, y_s) , and (x_c, y_c) denote the x and y coordinates of the mirror (or surface light is being reflected off), source, and camera as governed by the law of specular reflection. The distances d_{m2c} and d_{m2s} represent the absolute distance from the mirror to the camera and the mirror to the source, respectively. The distances z_{m2c} and z_{m2s} represent the distance along the optical axis from the mirror to the camera and mirror to the source, respectively. The surface sag, or null shape, is determined by $W(x_m, y_m)$.

By determining the geometrical locations of all of these components relative to one another it is possible determine the local surface slope in both the x and y directions through

Ritter's expression for surface slopes [4]. There are two main assumptions made in this approximation, the first being that the LCD, UUT, and camera are all coaxial, or $z_{m2s} \approx d_{m2s}$ and $z_{m2c} \approx d_{m2c}$. The second assumption is that the sag of the surface is relatively small in comparison to the testing distance, or that $z_{m2s}, z_{m2c} \gg W(x_m, y_m)$. Due to the surface sag playing a comparatively small role in the surface slope calculations, calibration of the system is primarily driven by the locations of the test components relative to one another. Calibration can be done through multiple different techniques using external coordinate measurement devices such as coordinate measuring machines (CMM's) or laser trackers.

$$S_y(x_m, y_m) = \frac{\frac{y_m - y_s}{d_{m2s}} + \frac{y_m - y_c}{d_{m2c}}}{\frac{z_{m2s} - W(x_m, y_m)}{d_{m2s}} + \frac{z_{m2c} - W(x_m, y_m)}{d_{m2c}}} \approx \frac{1}{2} \left(\frac{y_m - y_s}{z_{m2s}} + \frac{y_m - y_c}{z_{m2c}} \right) \quad (1)$$

$$S_x(x_m, y_m) = \frac{\frac{x_m - x_s}{d_{m2s}} + \frac{x_m - x_c}{d_{m2c}}}{\frac{z_{m2s} - W(x_m, y_m)}{d_{m2s}} + \frac{z_{m2c} - W(x_m, y_m)}{d_{m2c}}} \approx \frac{1}{2} \left(\frac{x_m - x_s}{z_{m2s}} + \frac{x_m - x_c}{z_{m2c}} \right) \quad (2)$$

Once the local surface slope has been measured across the UUT using Equations 1 and 2, integration of these local slope values allows for the surface height, and thusly the surface shape of the optic to be determined.

In deflectometry it is possible to focus on both the LCD and the UUT simultaneously, however for typical setups there is an intrinsic depth of field problem. This issue is alleviated through carefully selecting the fringes that are displayed, as demonstrated by phase-measuring deflectometry (PMD). Phase measuring deflectometry addresses the intrinsic depth of field problem by projecting a sinusoidal pattern of varying intensity values across the LCD screen and assigning a phase value to each individual pixel.

Since the sinusoidal fringes do not lose their phase information when they are not within the depth of focus, the UUT can be focused on while still reliably being able to determine individual pixel locations on the LCD display. When phase stepping the fringe pattern displayed known amounts and recording the $I_k(x, y)$ irradiance at each step, well defined reconstruction algorithms can be used to calculate the original phase values.

$$\Phi'(x_d, y_d) = \tan^{-1} \left(\frac{I_4(x, y) - I_2(x, y)}{I_1(x, y) - I_3(x, y)} \right) \quad (3)$$

Equation 3 is an example of a 4-phase step reconstruction, using the recorded irradiance at a pixel over four different phase steps to compute the phase value for that detector pixel. This recorded phase value is then matched with the corresponding phase value at the display source $\Phi(x_d, y_d)$. Due to the sinusoidal pattern oscillating in phase between values of $-\pi$ and $+\pi$, if more than one period is displayed there can be two different pixels with the same phase value, causing 2π ambiguity. This problem can be alleviated through means of unwrapping phase values over $-\pi \sim \pi$ on the wrapped phase, allowing for relative pixel-to-pixel tracking.

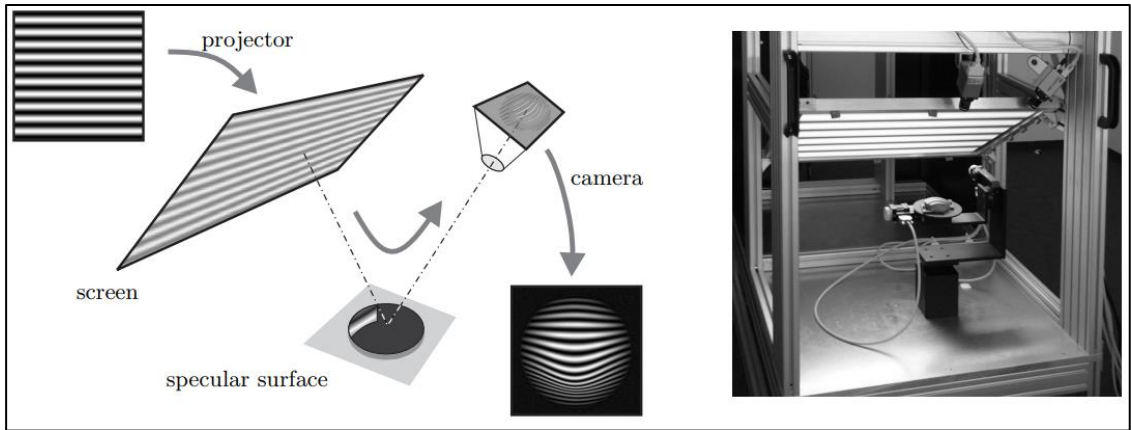


Figure 3. On the left side of the image a typical deflectometry setup based on PMD (figure from Markus C. Knauer et al. [3]).

Based on the illustration shown in Figure 3., each pixel has its own phase and position associated with it, which can then be accurately tracked while outside of the depth of focus of the camera. While a distorted image of the fringe pattern is created, the tracking of each individual pixel through its phase is how the surface slope is measured, not through analyzing the distorted image seen by the camera. The display patterns are projected across the screen horizontally and vertically to determine the local surface slope in the x and y directions. Uncertainty in distinguishing between the phases of two neighboring pixels is dependent not only on the spatial resolution capabilities of the camera, but also the contrast and the period of the sinusoidal pattern displayed. The phase uncertainty often decreases with higher contrast and as the period of the fringes gets shorter.

With the capability to accurately track each pixel location based on the phase information that it carries; it is possible to achieve highly accurate absolute surface measurements with a well calibrated system. However, it is possible to avoid a rigorous and typically timely calibration process and still achieve highly accurate surface measurements by systematically calibrating with a reference optic. By measuring a reference flat with the deflectometry system, it is possible to determine all systematic surface errors present at a specific position in space and automatically remove them from the flat test surface. This technique is one version of differential deflectometry, which alleviates some of the strict positional tolerances by looking at the differences between two similar samples.

$$\Delta S_y(x_m, x_y) = \frac{\frac{y_m - y_s}{d_{m2s}} + \frac{y_m - y_c}{d_{m2c}}}{\frac{z_{m2s} - W(x_m, y_m)}{d_{m2s}} + \frac{z_{m2c} - W(x_m, y_m)}{d_{m2c}}} - \frac{\frac{y'_m - y'_s}{d'_{m2s}} + \frac{y'_m - y'_c}{d'_{m2c}}}{\frac{z'_{m2s} - W'(x_m, y_m)}{d'_{m2s}} + \frac{z'_{m2c} - W'(x_m, y_m)}{d'_{m2c}}} \quad (4)$$

Equation 4 shows the difference in local surface slopes between two different samples. The variables hold the same meaning as those in Equations 1 and 2, with the prime variants holding similar meaning for a second measured surface. When measuring two nearly identical surfaces it is easy to see how the difference in local surface slopes is negligible, which is useful for measuring low-sag and flat optics. Specifically for the case of flat reference optics, the systematic error induced through misalignments in calibration can be completely removed from a test optic of similar shape and size.

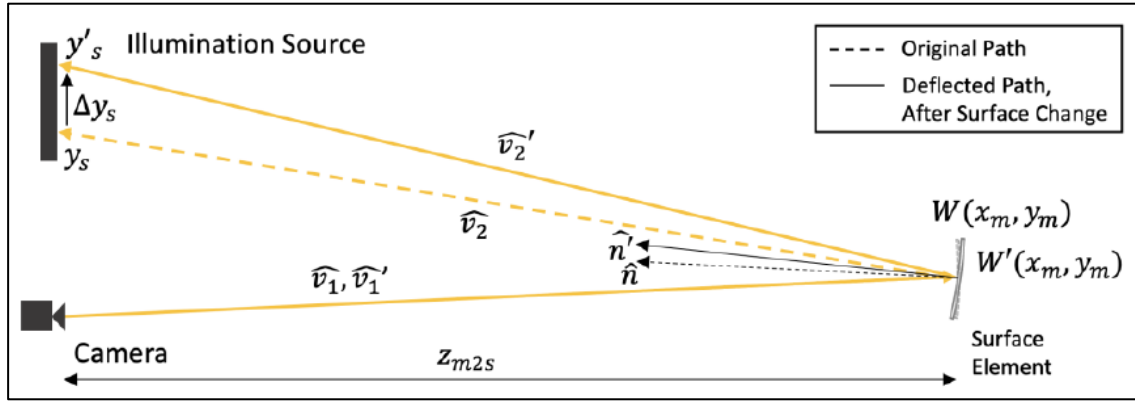


Figure 4. Basic concept of differential deflectometry illustrated (from Henry Quach et al. [5]). For surfaces that are flat/low sag and hold similar orientations, the difference in deflected path after surface change will be nearly negligible from the original path.

2.2 Interferometry

Interferometric optical testing is based on the phenomena of interference that occurs between two wavefronts of light. When two wavefronts of light meet the conditions for both temporal and spatial coherence the wave superposition principle combines the individual wavefronts simultaneously, exhibiting the property of constructive/destructive interference that creates fringes. An interferometer uses the differences between two wavefronts, a reference wavefront and a test wavefront, to determine the surface shape by recording and processing their interference patterns. The properties of a wave's frequency,

amplitude, and phase can be used to describe a particular wavefront of light and are thusly used to describe the interference pattern displayed between two different wavefronts. The most simplistic form of interference occurs between two monochromatic waves, also known as two beam interference.

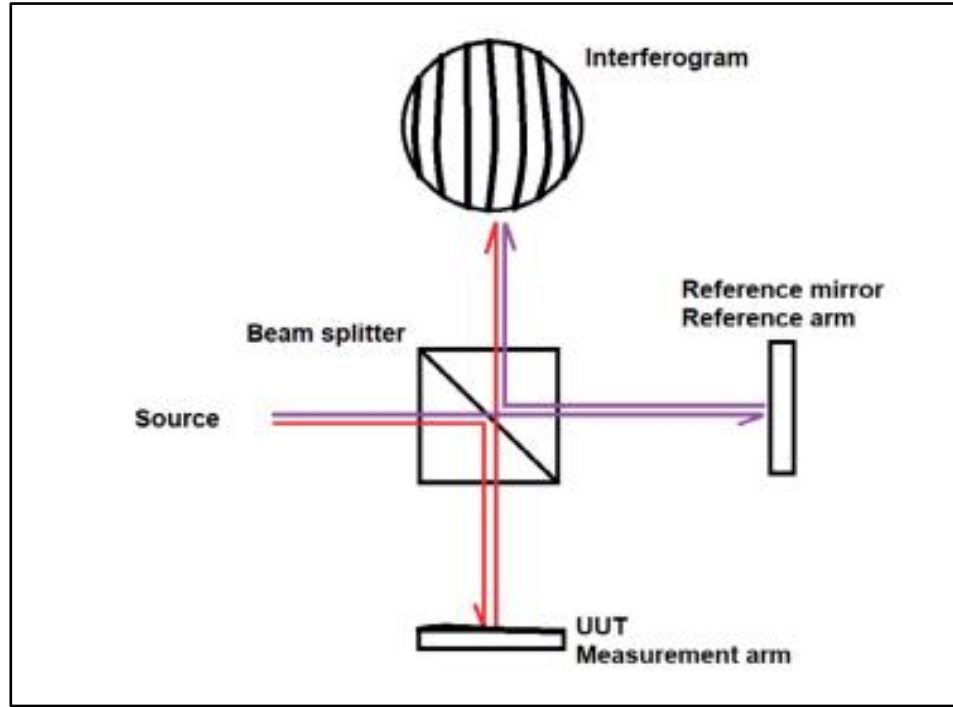


Figure 5. Traditional setup for interferometer that compares the wavefront difference between the reference wavefront (purple) and the UUT wavefront (red), causing an interference pattern known as an interferogram (from Jon Kam et al [6]). This interferogram contains information on the local phase variations between the UUT and Reference beam paths, which can be related to the local surface height through the optical path difference.

$$\phi(x, y) = k(x, y) \frac{2\pi}{\lambda} \left(\Delta z(x, y) \bmod \left(\frac{\lambda}{k(x, y)} \right) \right) \quad (5)$$

Equation 5 describes how the local phase $\phi(x, y)$ can be related to the OPD (Optical Path Difference) between the reference and measurement surfaces $\Delta z(x, y) = z_{obj}(x, y) - z_{ref}(x, y)$. λ is the central wavelength of the source, and $k(x, y)$ is a scaling factor that is dependent upon the geometry of the setup, being made a constant value when the surface

is at normal incidence relative to the detector. This scaling factor can become an issue when measuring surfaces with large surface sags, as it can produce retrace errors that require computer generated holograms (CGH's) to correct. For the case of low sag or flat optics this is not an issue [7]. This allows for accurate surface height measurements of the UUT that is scaled in units of the wavelength of the source. Single wavelength interferometry can be extremely accurate through phase shifting techniques; however, it suffers from discontinuity in fringes at surface structures that have large steps or discontinuities, which makes it impossible to know how many full waves of OPD difference there are. By using two wavelengths the dynamic range can be increased to the equivalent wavelength λ_{eq} [10], however this increase in source spectrum decreases the coherence length. In the case of White Light Interferometry (WLI) the broad spectrum of frequencies that are used for the source is to the benefit of the axial resolution of the system.

For systems using the interference of light to map the topography of a system the coherence length, or coherence time, defines the axial length in which a source can still produce fringes. As long as the OPD between two wavefronts is less than the coherence length fringes can be produced, and the surface can be measured. In the case of WLI, shown in Figure 6., the coherence length is short due to the broad spectrum of the source, meaning that accurate surface height measurements can be made over a large dynamic range due to its scanning functionality and unique interferogram processing. Through use of vertical scanning methods many individual pixel measurements are made over a field of view and used to measure the surface height of the UUT. Both the FoV and scan length are adjustable, making it a versatile metrology method for measuring various surface shapes and/or surface structures at the expense of measurement time.

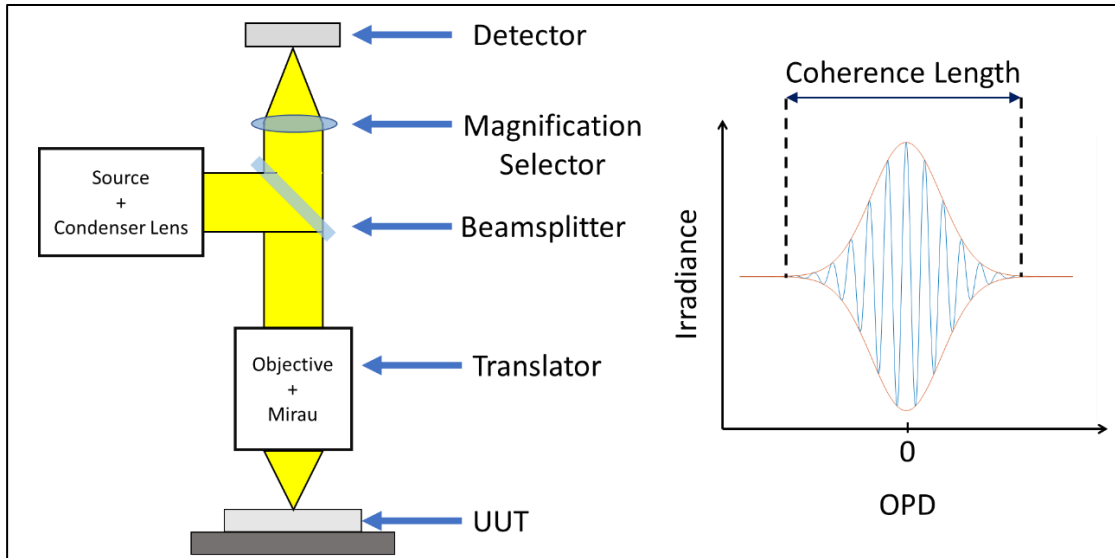


Figure 6. Illustration of typical vertical scanning or coherence probe interferometers (left) and individual pixel measurement while scanning (right) (Inspired by James Wyant et al. [8]).

Chapter 3. Data Collection Process and System Calibration

The surface measurements are performed on two different systems, a system for deflectometry measurements and a system for WLI measurements. The deflectometry system constructed in the Large Optics Fabrication and Testing group's lab is used to obtain accurate low-order frequency measurements of the test surface through use of the software SCOTS [9]. The WLI system is a Zygo NewView™ 9000 that makes use of Python as an API that allows for customizable sub-aperture collection methods. Zaber linear translation stages are used to obtain the sub-aperture positions during the WLI surface measurements to ensure the sub-aperture positions are accurate, which is important in the surface stitching process. The UUT being measured is a 7×7 mm clear aperture of a larger Ø50.8 mm Fused Silica Mirror blank. On this UUT are two fiducials that are shaped similar to gaussians in order to be used as datums for the fiducial stitching process. These fiducials are also used as a means of validating the capabilities of the merging techniques.

The fiducials are created on the surface of the UUT in order to establish common positional reference datums for both the WLI and deflectometry data sets that are beneficial for aligning and accurately stitching the sub-aperture maps. The width and depth of the fiducials are determined by the dynamic ranges of both the deflectometry and WLI setups.

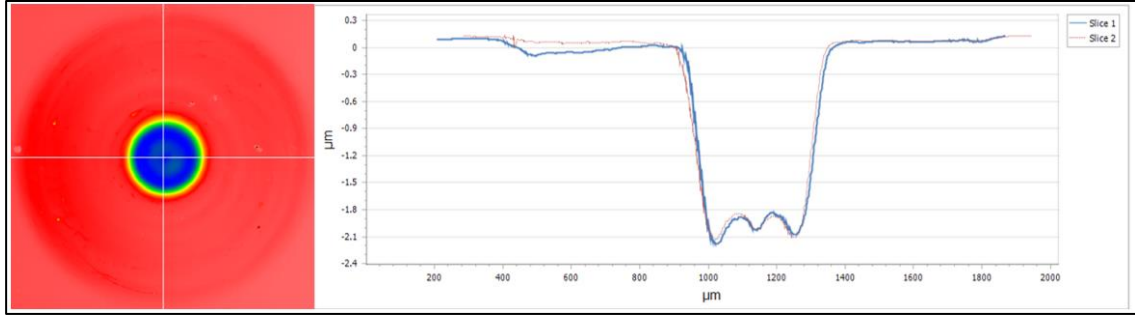


Figure 7. On the Left is the central fiducial fabricated on the UUT surface with two slices going through the center as to confirm symmetry of the fiducial (measured with WLI). On the right are the two surface slices representing the shape of the fiducial. Although the fiducial is not a perfect gaussian shape, it is still suitable as a datum.

The WLI is used to measure the UUT in order to determine the higher order shape of the surface. A 1.6×1.6 mm FoV (maximum for current setup) was used to measure the entirety of the UUT through many individual sub-apertures, using minimal overlap between sub-apertures as to speed up the data acquisition process. The time taken to measure the entirety of the UUT was not tracked throughout the data acquisition process, however minimal overlap regions were used as to model a realistic data acquisition scenario. Masashi Otsubo et al. [2] demonstrates that as the overlap region between two neighboring sub-apertures increase, the uncertainty exponentially decreases in tip, tilt, and constant phase shift induced by vertical/horizontal movement of the data. Even though large overlap between sub-apertures mitigates the stitching error, the large number of sub-apertures needed to measure the surface could still induce low-order shape error in the stitched map.

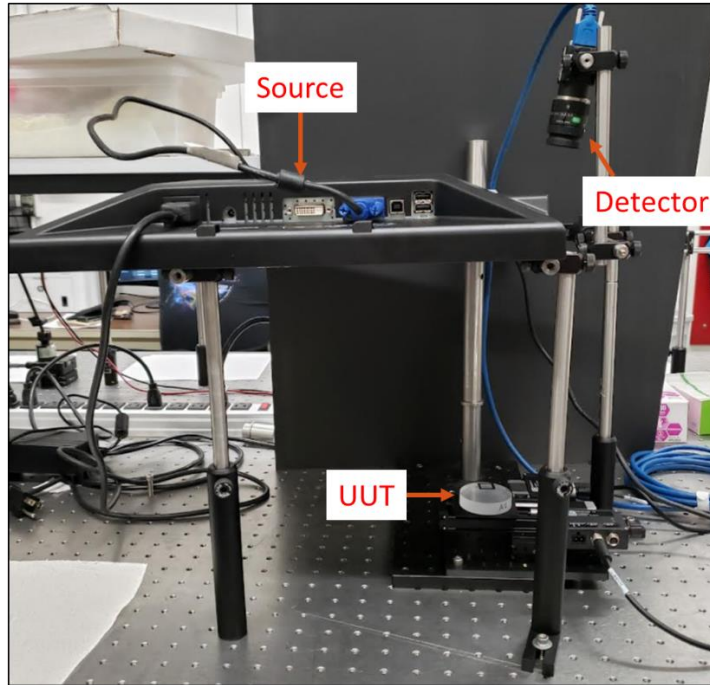


Figure 8. Deflectometry setup constructed showing the source, UUT, detector, and motorized linear translation stages used for deflectometry sub-aperture measurements.

3.1 Deflectometry Calibration

Before any surface measurements are made using the deflectometry system, calibration is established in two phases: 1) calibration of the systematic errors due to the off-axis layout of camera-UUT-monitor and the unknown aberrations of the camera system 2) calibration of the linear translation stages. For the deflectometry system, an optical flat window is utilized as a reference to measure for the differential deflectometry system calibration. The systematic add-up error on the surface map is removed by taking a series of reference measurements using the reference optical flat, and then subtracting them out of the UUT map in the post data processing. This allows for the true surface shape to be measured every time. Figure 9. displays the consistency between measurements of the same optical sample, showing discrepancies between the two measurements to be on the scale of 10's of nanometers.

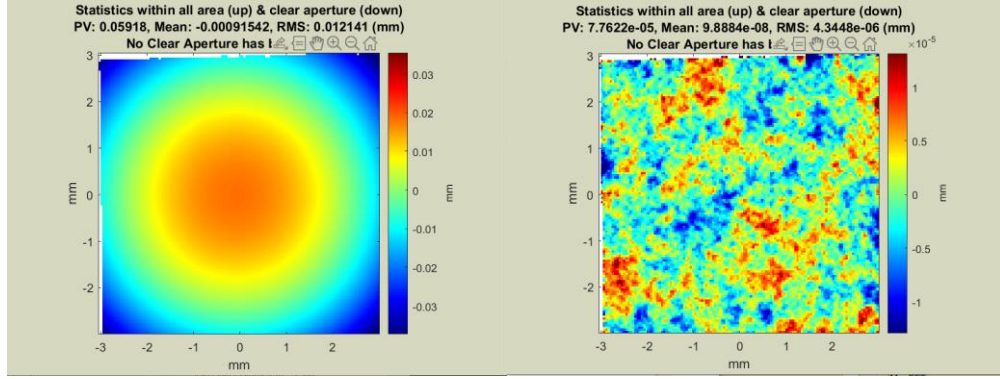


Figure 9. Deflectometry sub-aperture measurement before calibration (left) and after calibration (right). High frequency residuals induced by gaussian noise of the monitor and CMOS are all that remains after this differential deflectometry calibration technique. The size of the reference data is 140×140 pixels ($\sim 7.0 \times 7.0$ mm), the same as the map of the UUT.

3.2 Motorized Translation Stage Calibration

The calibration of the movement of the motorized translation stages is achieved through tracking a fiducial over a series of precise movements using the camera for the deflectometry system. To reduce effects of aberrations from the camera, such as distortion, from impacting the calibration data the fiducial is moved to the center of the field of view and marked as the origin point at the image of the camera. The fiducial is then translated ± 2 mm in the x and y directions separately, having its physical position recorded as well as its camera pixel centroid position. The orthogonality of the CMOS pixel array is used to evaluate orthogonality of the x and y axis of translation stage. This movement is done one step at a time in order to find the angular deviation between each axis of the linear translation stages, find the difference between the coordinate frames of the translation stages and the camera, and determine the pixel pitch per unit distance.

Chapter 4. Data Analysis and Metrology Data Merging

Merging the deflectometry and WLI data sets is done as to use the best and most reliable information from each metrology method. By using the deflectometry data as the low-frequency foundation that the high-frequency WLI data can be placed upon, the error in unreliability induced during the sub-aperture stitching process is corrected for. Two separate approaches for the data merging process were implemented during this study; one that merges the data sets by means of polynomial fitting in the spatial domain and one that merges the data sets by means of frequency fusion in the spatial frequency domain.

4.1 Polynomial Fitting and Merging

The polynomial fitting approach is performed by matching the piston tip/tilt terms present in each WLI sub-aperture to the deflectometry map in its respective overlap region. Each WLI sub-aperture has its low-order terms determined through polynomial fitting the data in the region that it overlaps with its neighboring sub-aperture. These two sets of low-order terms, corresponding to the piston tip/tilt, are then matched to one another as to create a single continuous stitched map. This stitched WLI map is then merged to the deflectometry data by matching the piston tip/tilt data from the stitched WLI map to the low-order data of the deflectometry map. This process is repeated for each WLI sub-aperture, eventually leading to a stitched WLI map over the UUT in which the low-order WLI terms match the low-order deflectometry data. In other words, the low-order shape of the stitched map comes from the polynomial coefficients of the deflectometry data, with these coefficients corresponding to the piston tip/tilt of the WLI sub-apertures.

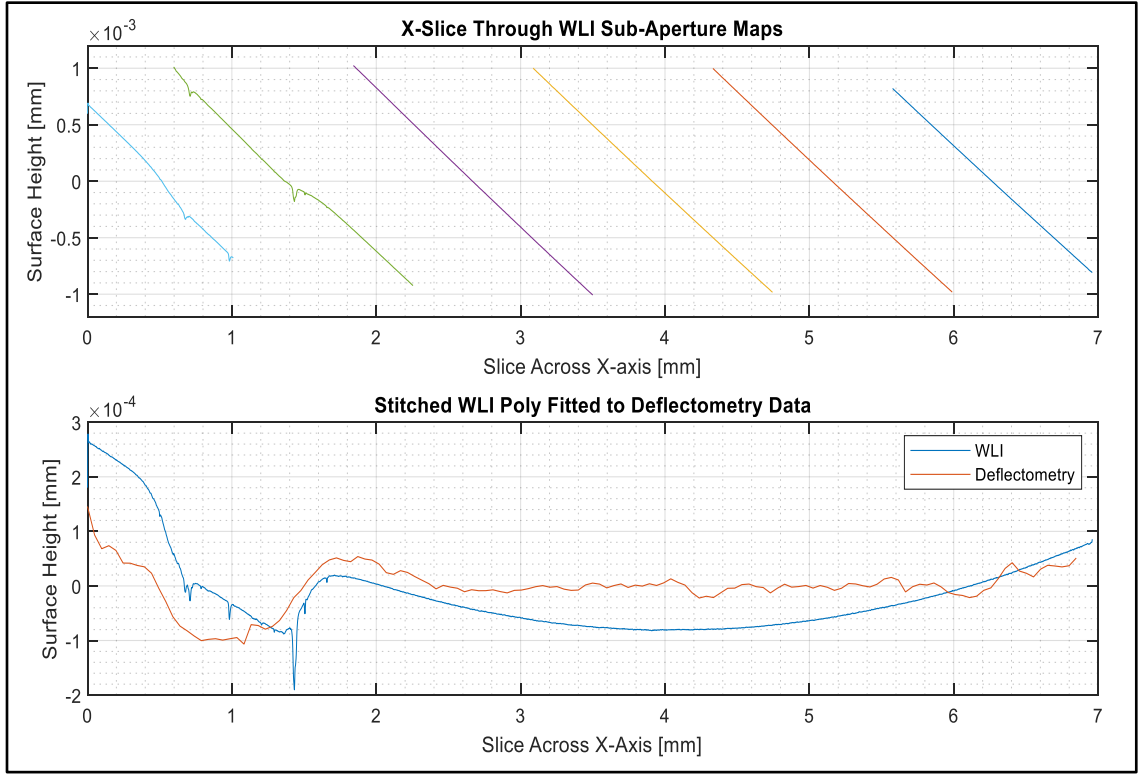


Figure 10. (Top Plot) X-Slice across each individual sub-aperture before stitching. (Bottom Plot) X-Slice of original deflectometry data with stitched and polynomial fitted WLI data.

Figure 10. shows the completed polynomial sub-aperture stitching process starting from the original WLI sub-aperture data to the stitched and merged WLI map in comparison to the original deflectometry map. This approach does produce more reliable low-order data on the side of the stitched WLI map, however it is still limited in its ability to meet the deflectometry data. Correction of the piston tip/tilt during the stitching process is not sufficient to encapsulate the entirety of the low-order information from the deflectometry data. This rigid limitation however does not exist when fusing the two maps together in the spatial frequency domain.

4.2 Frequency Domain Merging

Merging the two data sets together in the spatial frequency domain is performed by using the deflectometry data as the basis for the low-order frequency information and using the WLI data as the basis for the higher-order frequency information. This means that we must select where the cutoff for low-order frequency data ends (deflectometry frequency zone), and where the high-order frequency data begins (WLI frequency zone). This process can be performed in two ways; we may either use all spatial frequencies from the deflectometry data and continue past that with the spatial frequency information from the stitched WLI data, or we may use only a section of the deflectometry spatial frequency information. For the initial investigation into this process 20.3 cyc/mm (maximum spatial frequency of deflectometry data) was used as the cutoff for the low-order frequency information taken from the deflectometry data, and 20.3 cyc/mm through 616.9 cyc/mm from the WLI data was used as the basis for the mid to high spatial frequency information.

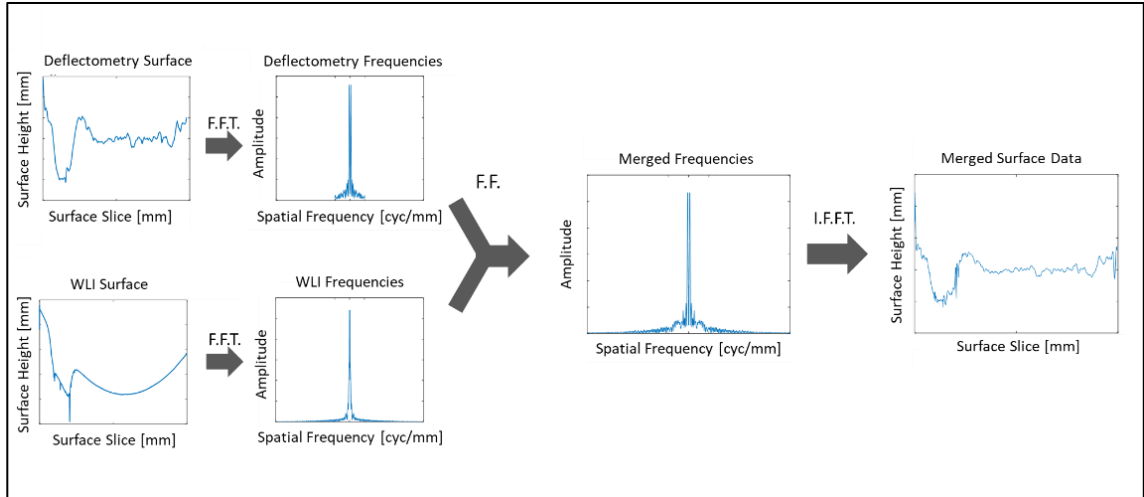


Figure 11. Illustration of workflow in order to merge deflectometry and WLI data through Frequency Fusion. The original deflectometry and WLI data are decomposed into their spatial frequency terms, and then combined. This fused frequency map is then returned to the spatial domain in order to achieve the merging between the two data sets.

As illustrated in Figure 11., the deflectometry data sets and the WLI data sets are separately Fourier Transformed and then combined through frequency fusion in order to get one complete set of merged frequencies. For this merging process, the spatial frequencies in the low-order range are taken from the deflectometry data and placed into the frequency spectrum of the WLI data. The merged frequency data is then inverse Fourier Transformed and the merging between the two data sets is complete. However, since we are using a Fast Fourier Transform there is an inherent assumption that the sampling between spatial frequencies is the same, which is untrue for the combined frequency data. The mismatching in spatial frequency sampling leads to an error in the phase of the merged frequencies, leading to the data being slightly shifted in the spatial domain, as shown in Figure 11. To account for the issue of the mismatching spatial frequencies sampling, the two original data sets are zero-padded to make the frequency sampling of the two data sets the same. In equation 6. the sampling of the spatial frequencies is determined by the cutoff

frequencies (f_{deflect} and f_{WLI}), the number of data points in the original data sets ($size_{\text{deflect}}$ and $size_{WLI}$), and the integer amount of zero-padding added to each original data set (pad_{deflect} and pad_{WLI}). By satisfying the equation for the amount of zero-padding required in both data sets the sampling of the two spatial frequencies is the same, and the phase error no longer occurs.

$$\frac{f_{\text{deflect}}}{size_{\text{deflect}} + pad_{\text{deflect}}} = \frac{f_{WLI}}{size_{WLI} + pad_{WLI}} \quad (6)$$

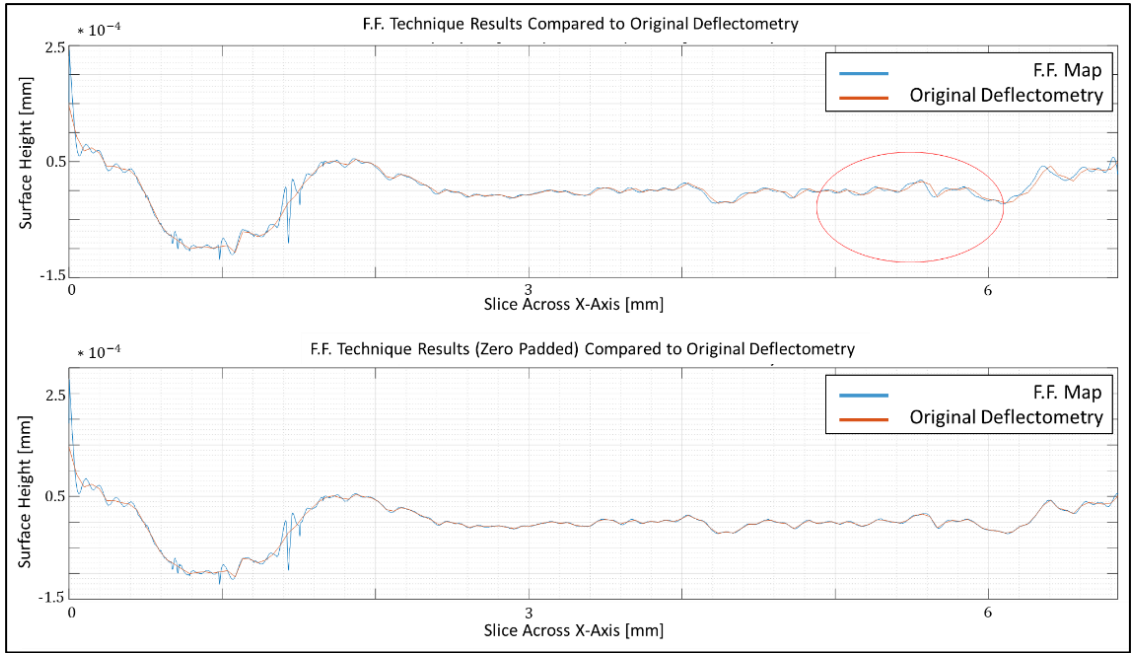


Figure 12. Frequency Fusion technique being compared to original deflectometry data with no zero-padding (top) and with zero-padding that satisfies equation 6. (bottom). The region circled in red indicates where the shifting effect is most prominent. The zero-padded case shows that the frequency fusion technique fits to the low-order deflectometry data extremely well. In this figure the values used were $f_{\text{deflect}} = 20.3$, $f_{WLI} = 616.9$, $size_{\text{deflect}} = 140$, $size_{WLI} = 4294$, $pad_{\text{deflect}} = 469$, $pad_{WLI} = 14213$.

Comparing the results between the polynomial and frequency fusion data merging techniques, the frequency fusion method produces more promising results when merging

the two data sets together due to its ability to fit to the deflectometry data more firmly. This is due to the low-order spatial frequency terms consisting of more than just the piston tip/tilt data that the polynomial merging method is constrained to. The control over which frequencies are used from each of the different data sets adds to the versatility of this methodology.

4.3 Low and High-Pass Filter Masks

As discussed previously the cutoff for the low-order deflectometry data can be any spatial frequency up to the cutoff frequency of 20.3 cyc/mm, which is the maximum frequency of the deflectometry data. When combining the two data sets in the Fourier domain, low and high-pass filters are employed through use of masks. These masks are defined by their application radii (ρ_1 and ρ_2) as to accurately select the desired weighting functions of the frequencies that the filters span over. Three different masks are applied independently to both sets of data as to study their effects on the frequency fusion process: (1) Flat Top, (2) Ramp, (3) Flat Top (high-order) Gaussian. These various masks are chosen due to how they uniquely merge the data sets. The Flat Top Mask fuses the frequencies using Boolean values to determine when the deflectometry information ends and where the WLI information begins. The Ramp and Gaussian Masks fuse the data sets together by selecting a window region where values from both data sets are combined with different weights on each. The summation of these combined high and low-pass weighting functions is '1' across all spatial frequencies. Selecting where the cutoff in frequencies occurs allows for the most trustable data from each metrology method to be used, enabling us to fit the data as desired. This is particularly useful when looking at an area of interest, such as the fiducials, that contain both high and low-order frequency data.

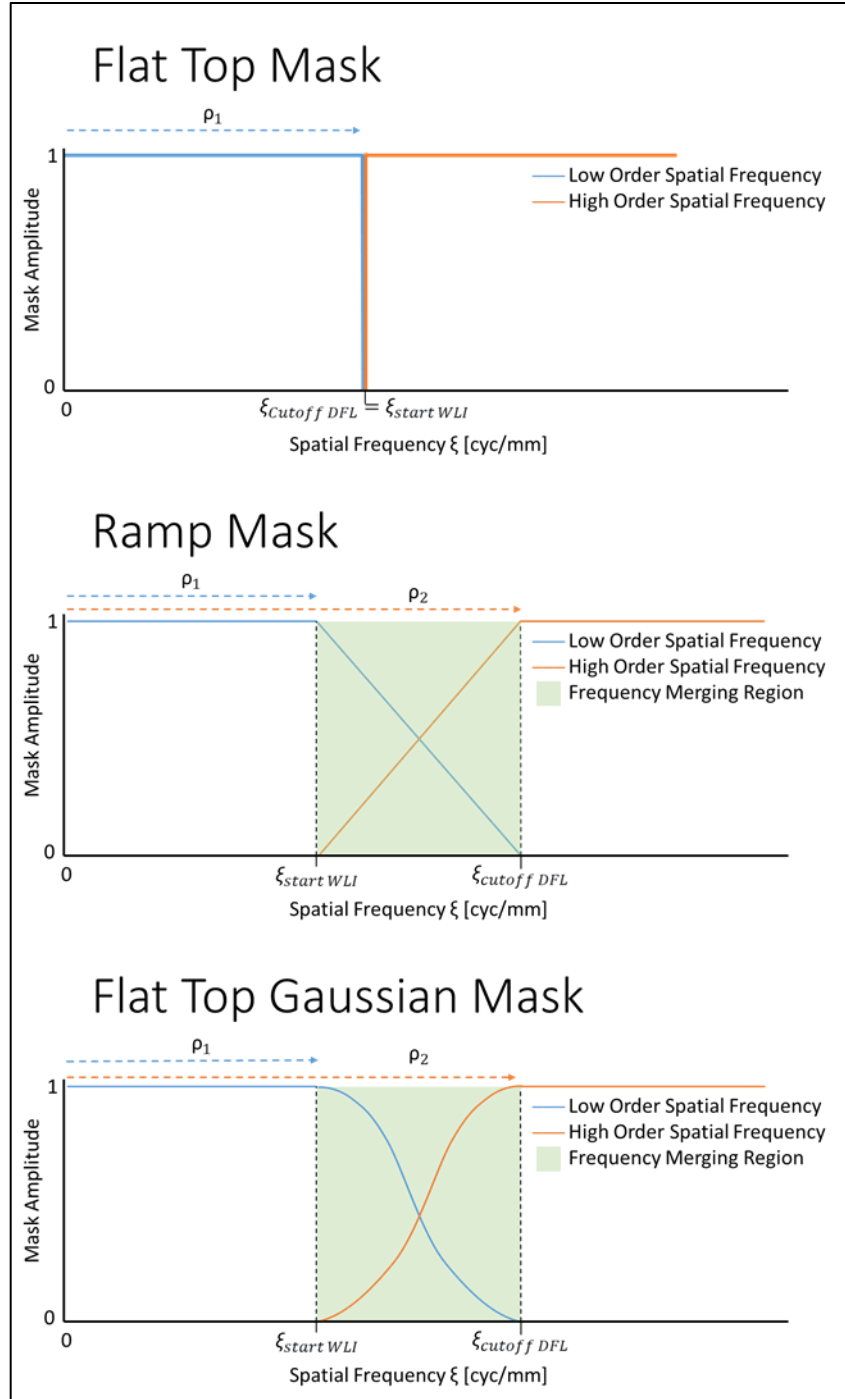


Figure 13. Masks used during the frequency fusion process. ρ_1 and ρ_2 represent adjustable parameters that determine the range where the weightings on frequency are unity (ρ_1) and the range of frequencies included in the low-pass filter mask (ρ_2). The high-pass filters are the exact opposite of the low-pass filters. The green region shown is where the deflectometry and WLI frequencies merge together, with their weighting on the frequencies in that region determined by their respective functions. This region does not exist for the Flat Top Mask since the transition between data sets is abrupt. The sum of the combined high and low-order spatial frequency weighting functions is unity everywhere.

Figure 13. shows the various masks used for the frequency fusion process. The low-pass filter is defined by the application radii ρ_1 and ρ_2 . Parameter ρ_1 determines the span of frequencies where the filter weighting is unity, and parameter ρ_2 determines where the low-pass filter ends. Between the two radii is where mixing between the low and high spatial frequencies occurs, with the weightings on the frequencies determined by the mask being applied. Since the combined weightings over the span of spatial frequencies included in both filters must be unity, the high-pass filter is simply the opposite of the low-pass filter.

With the low-pass filter defining the low spatial frequencies, and the high-pass filter defining the high spatial frequencies, they are combined to create a complete frequency spectrum. Each of the masks, with the exception of the Flat Top, defines a different weighting function in the frequency merging section. As is for the entirety of the spatial frequency spectrum, the summation of the weights applied by the low and high-pass filters in this merging section adds to equal unity. The application radii and weighting functions in the merging section determine how smooth the transition is between spatial frequency filters, the effect of which can be seen particularly in the case of the Flat Top Mask that contains no merging section.

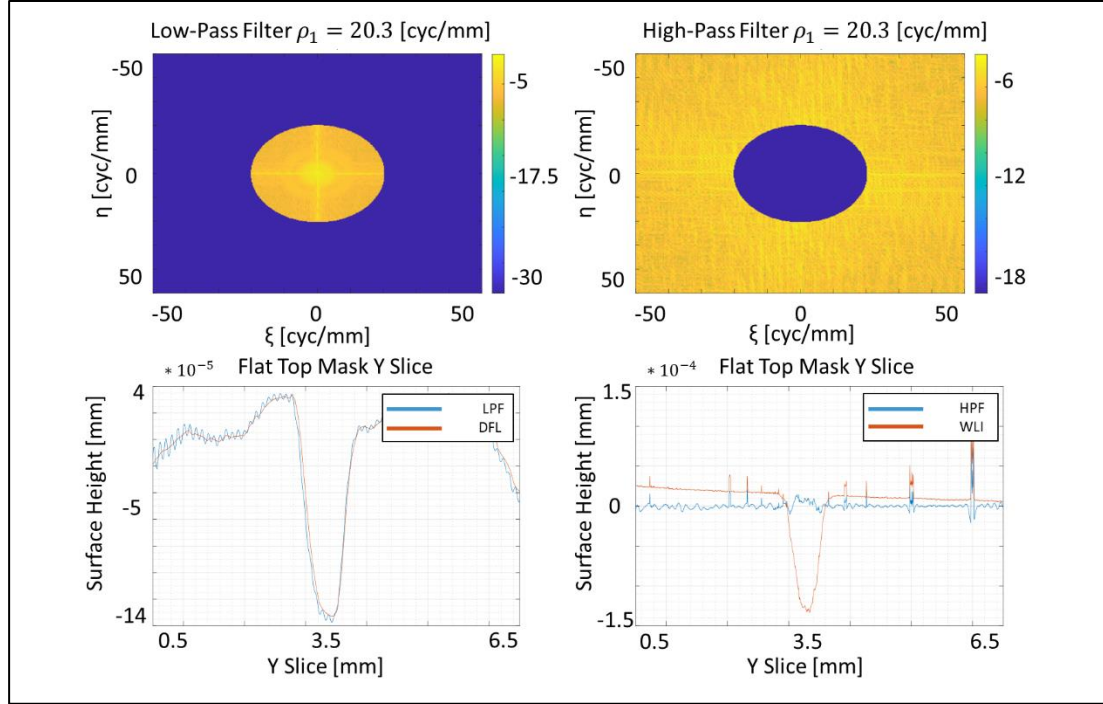


Figure 14. Low-pass (LPF) and high-pass filters (HPF) for the Flat Top Mask applied to the WLI and deflectometry spatial frequencies separately, amplitudes are scaled logarithmically. The low-pass data (left) is compared to the original deflectometry (DFL) data, and the high-pass data (right) is compared to the original WLI data to determine how well they hold their respective low and high-order frequency information.

Figure 14. shows the low and high-pass filters created by the Flat Top Mask for $\rho_1=20.3$ cyc/mm. While the low and high-order frequency information is held between their respective filters, the abrupt cutoff between the low and high-pass filters creates a rippling effect seen in both surface data sets. As shown on the left side of the figure, the inverse Fourier transform of the cropped out spatial frequency region created by the mask produces ripples that did not exist in the original data. These ripples are prominent due to the jump between the high and low-order frequency information, without a region in which a smooth transition may occur unwanted artifacts are expected. This jump in frequencies is noticeable when looking at a cross-section of the merged frequency map.

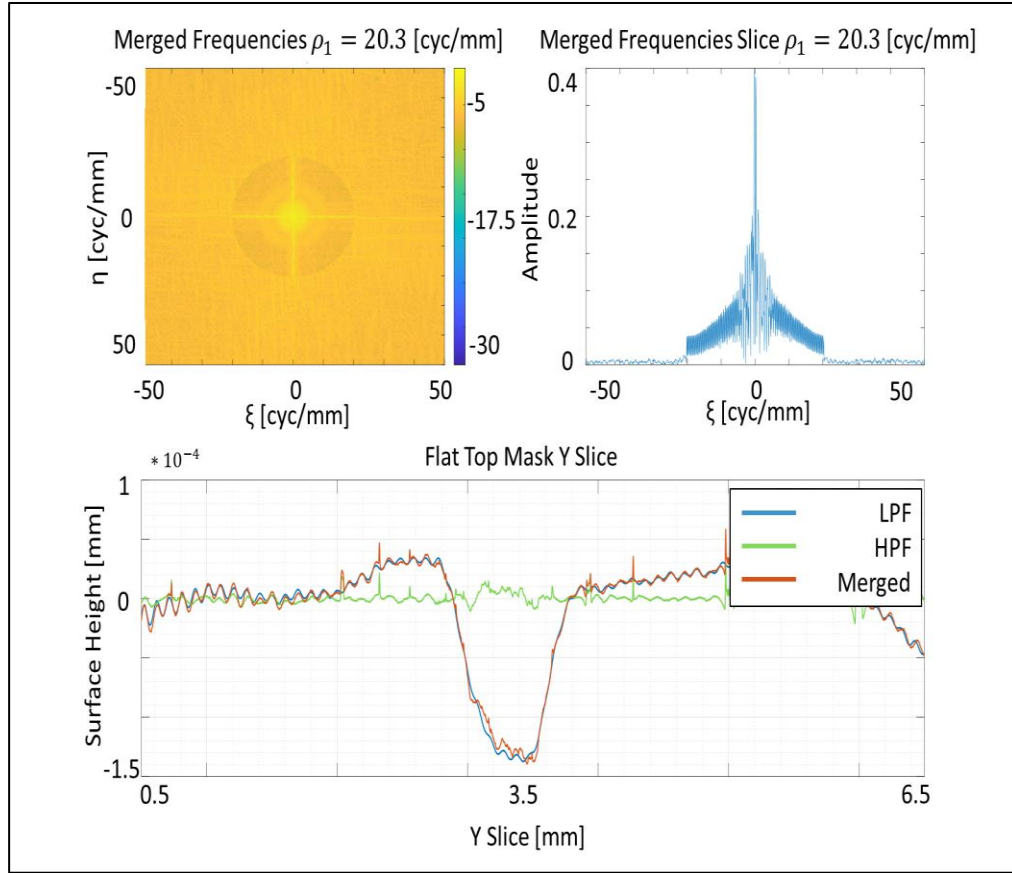


Figure 15. Spatial frequency merging of the low and high-pass filters produced by the Flat Top Mask (top left), slice along center of merged frequency map with normal amplitude scaling (top right), and merged surface data (bottom).

Figure 15. shows the addition of the low and high-pass filters created by the Flat Top Mask, and the results of the merged surface data. The cross-section slice of the merged frequency map shows the jump between the low-order and high-order spatial frequencies. This jump in frequencies leads to the rippling effect seen in the individual low and high-order surface maps, as well as the merged map. This undesirable rippling due to the abrupt cutoff in spatial frequencies is due to how the filters are applied. For the low-pass filter a Boolean circular function is multiplied with the original spatial frequency information, which is the same as convolution with a sombrero function in the spatial domain. This

rippling effect can be eliminated through proper frequency transition in the merging window.

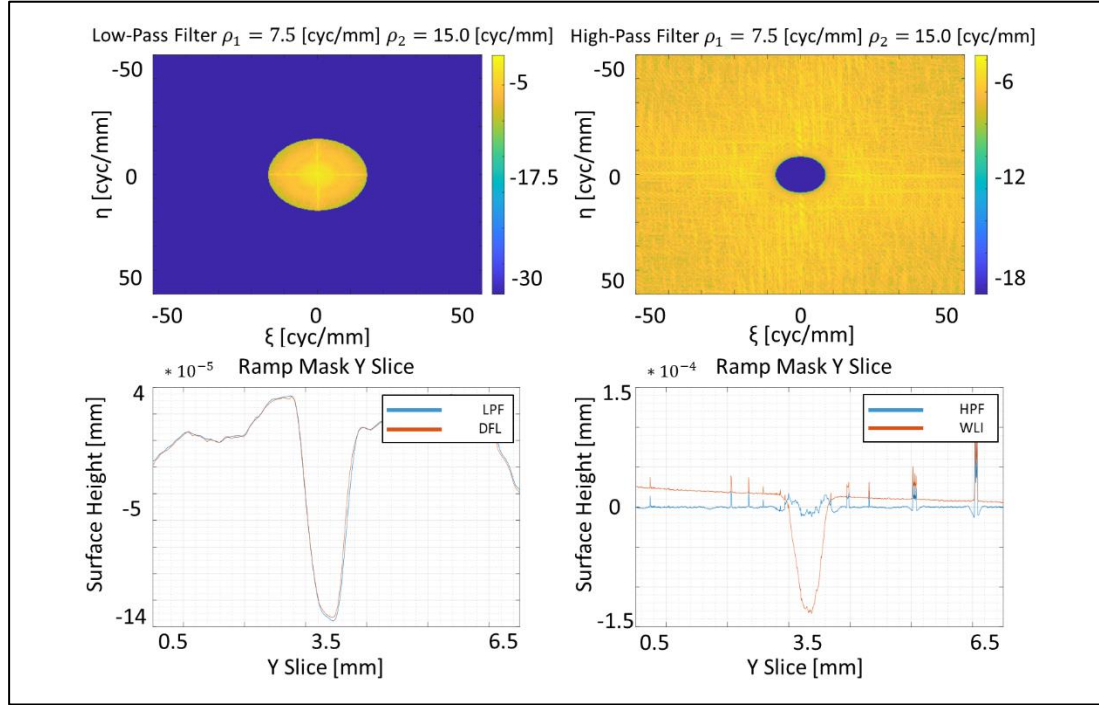


Figure 16. Low-pass and high-pass filters for the Ramp Mask applied to the WLI and deflectometry spatial frequencies separately. The low-pass data (left) is compared to the original deflectometry data, and the high-pass data (right) is compared to the original WLI data to show how they maintain their unique shape characteristics. The rippling effect produced by the sharp cutoff in spatial frequencies is no longer seen due to the merging window between ρ_1 and ρ_2 .

Figure 16. shows the low and high-pass filters produced by the Ramp Mask for $\rho_1=7.5$ cyc/mm and $\rho_2 = 15.0$ cyc/mm. Although the span of frequencies that the low and high-pass filter varies from that of the Flat Top Mask, a similar consistency in the low and high-order shapes can be seen. The rippling effect seen previously from the application of the Flat Top Mask is negated for both the low and high-order surface shape due to the gradual merging between the two filters. The weighting function applied over the merging region is a ramp function, which produces desirable results due to its ability to smoothly

combine the high and low-order data in the merging region.

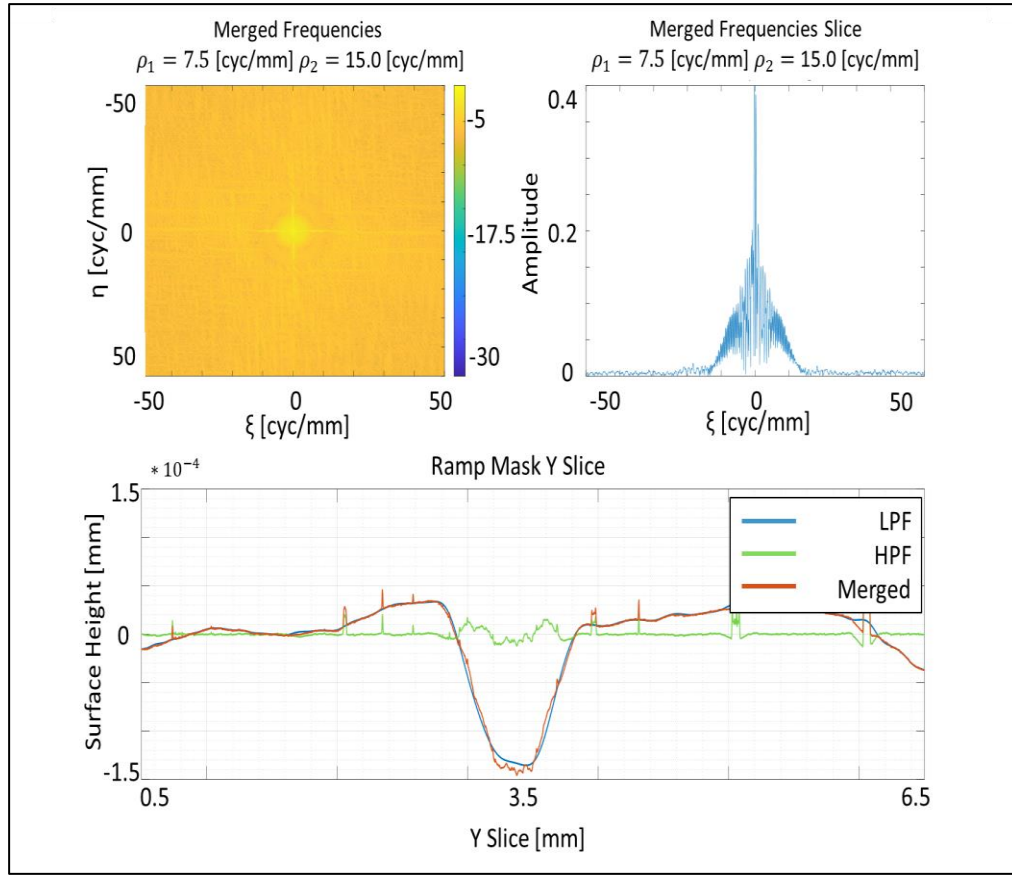


Figure 17. Spatial frequency merging of the low and high-pass filters produced by the Ramp Mask (top left), slice along center of merged frequency map (top right), and merged surface data (bottom).

Figure 17. shows the results of merging the low and high-pass filters for the case of the Ramp Mask with parameters $\rho_1=7.5$ cyc/mm and $\rho_2 = 15.0$ cyc/mm. In a stark contrast to the Flat Top Mask shown in Figure 15., the slice through the center of the merged spatial frequencies shows a smooth transition between the low and high-order information, producing a merged surface with no residual ripples. The merged surface slice demonstrates good matching to both the low and high-order surface shape.

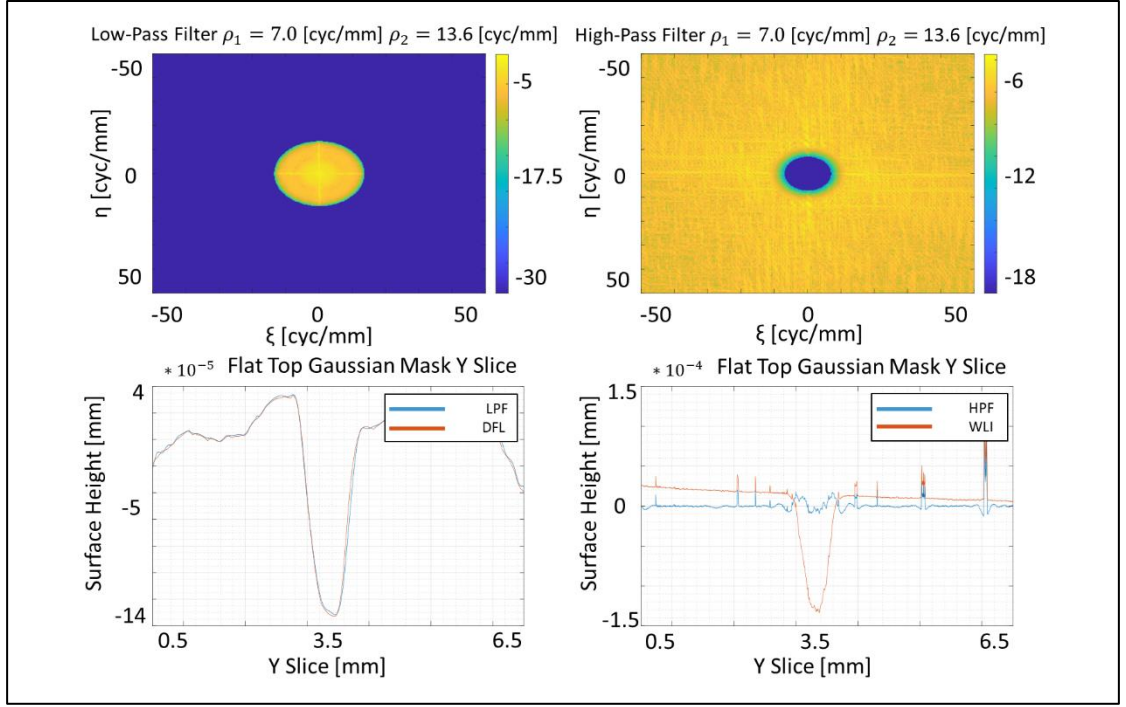


Figure 18. Low-pass and high-pass filters for the Flat Top Gaussian Mask applied to the WLI and deflectometry spatial frequencies separately. The low-pass data (left) is compared to the original deflectometry data, and the high-pass data (right) is compared to the original WLI data to show how they maintain their unique shape characteristics. The Rippling effect produced by the sharp cutoff in spatial frequencies is greatly reduced, however not completely negated due to the transition window being somewhat abrupt.

Figure 18. shows the results for the low and high-pass filters produced by the Flat Top Gaussian Mask for the parameters of $\rho_1 = 7$ cyc/mm and $\rho_2 = 13.6$ cyc/mm. Due to the nature of the Flat Top (high-order) Gaussian having a value of ‘1’ only at the center and a value of ‘0’ at infinity, characterization values for the weighting function were used to determine the values of ρ_1 and ρ_2 , being 0.999 and 1×10^{-4} respectively. While the vast majority of the rippling effect is negated due to the smooth transition in the frequency mask, there are still residuals seen in the low and high-order frequency information that is not present in the Ramp Mask. This is due to the Flat Top Gaussian Mask shown in Figure 18. having a somewhat steep weighting transition between the low and high-pass filters. This

could be reduced by further adjusting the weighting radii parameters; however, this proper overlap window region is slightly more difficult to determine in comparison to the linear ramp function.

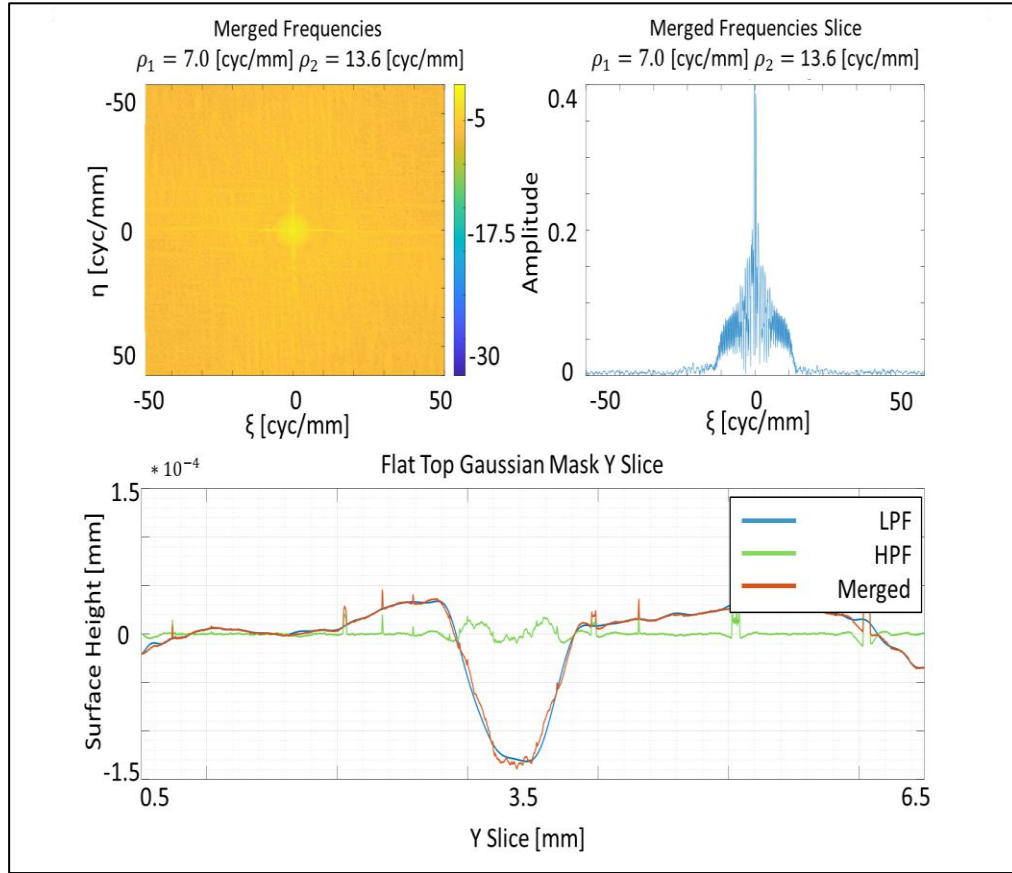


Figure 19. Spatial frequency merging of the low and high-pass filters produced by the Flat Top Gaussian Mask (top left), slice along center of merged frequency map (top right), and merged surface data (bottom).

Figure 19. shows the results of merging the low and high-pass filters for the case of the Flat Top Gaussian Mask with parameters $\rho_1=7$ cyc/mm and $\rho_2 = 13.6$ cyc/mm. As seen in the merged frequency slice, the merging between the high and low-order data is quite smooth in comparison to the Flat Top Mask, however it becomes steep at the end causing a somewhat abrupt transition. The results of this are seen in the lower frequency ripples

across both the low and high-order data.

When selecting the overlapping window for the frequency fusion process, the reliability in both filter's overlapping frequencies must be considered. Ideally, in the case of well calibrated deflectometry and WLI data, there is an overlap in spatial frequencies that is trustable for both data sets, but perhaps not completely trustable. The reliability in the WLI or deflectometry data may not be 100% always, it may decrease in a linear trend, gaussian trend, or another mathematical trend. Various masks can create low and high-pass filters with weighting functions that coincide with the reliability of the spatial frequencies spanned in the overlap region. The ability to modify the weighting function in the overlapping region, as well as the adjustability of the overlapping window, makes the frequency fusion method exceptionally flexible.

4.4 Mask Application Adjustability

As discussed previously, the form that the low and high-pass filters take can be adjusted by varying the parameters ρ_1 and ρ_2 . This adjustability allows for the merged map to better fit the deflectometry or WLI data as desired. This is useful when fitting to what data is considered to be most “trustable”, especially so when looking at areas of interest like the fiducials. The WLI data is considered to be more trustable in comparison to the deflectometry data due its ability to properly sample the fiducial. For the purposes of displaying this adjustability to fit the data sets as desired, the Ramp Mask is used due to its consistency in performance in comparison to the Flat Top Gaussian Mask.

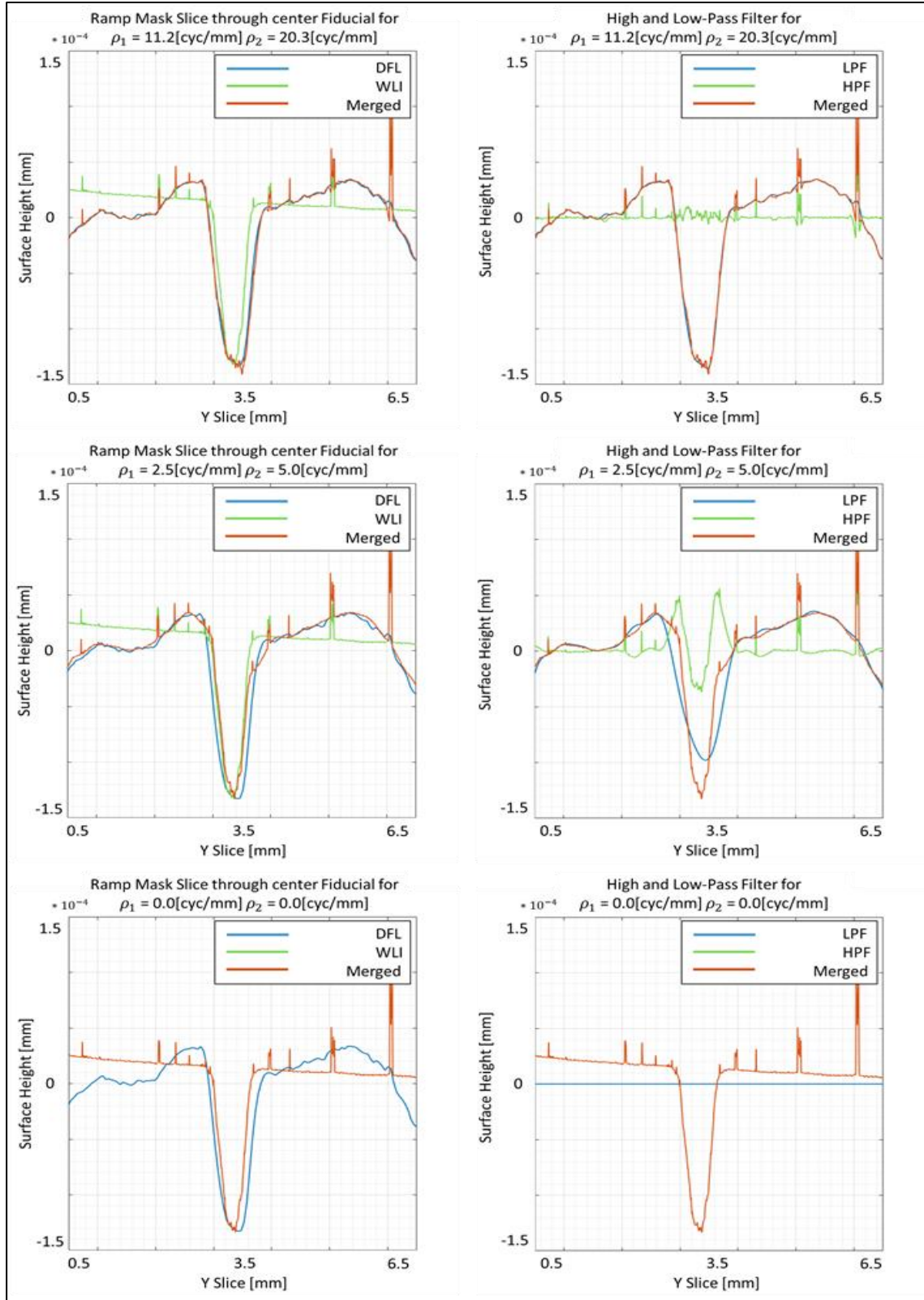


Figure 20. Results of merged frequency information (left) and individual low and high-pass filter components (right) for multiple values of ρ_1 and ρ_2 .

Figure 20. displays the ability for the low and high-pass filters to span different spatial frequencies as desired. On the left side of the figure are the merged results (orange) being compared to the original deflectometry data (blue) and the original WLI data (green). On the right side of the figure is the surface data information contained by the low-pass filter (blue), high-pass filter (green), and the merged data results (orange). For the case of $\rho_1 = 11.2$ cyc/mm and $\rho_2 = 20.3$ cyc/mm the merged data information is seen to match the raw deflectometry data closely. When looking at the surface information that comes from the low-pass filter the majority of the low-order data is present, and when looking at the surface information that comes from the high-pass filter all of the high-order data is present. As the frequency spectrum of the low-pass filter decreases, as is for $\rho_1 = 2.5$ cyc/mm and $\rho_2 = 5.0$ cyc/mm, the low-order information is no longer primarily defined by the deflectometry data. It is seen that the majority of the surface information is contributed from the WLI data, making the merged data set more closely match the raw WLI data. In the final case the low-pass filter is completely turned off, showing that both the low and high-order surface information is contained within the high-pass filter. This is why the high-pass filter is the exact same as the merged data, and why the merged data exactly matches the raw WLI data. By adjusting the values of ρ_1 and ρ_2 , as well as the function used to define the merging region between low and high-pass filters, the merged data information can more closely match that of the WLI or deflectometry data sets as desired. These results exhibit the adaptability and robustness of the frequency fusion methodology.

4.5 Verification Through Synthetic Data Evaluation

The merged surface created through use of the frequency fusion masks consists of information from both the WLI and deflectometry data sets, creating a new surface that

cannot be directly compared to either. This makes it difficult to know if any false surface information is created through application of the masks. In order to confirm that the frequency fusion masks were not causing any errors in the merged surface data, the Ramp Mask was applied to a synthetic data set comprised of the first 500 Zernike terms (with random values applied to each term). Figure 21. shows that any errors produced by application of the frequency fusion masks are negligible, with differences between the original and frequency fused surfaces being on the scale of 1×10^{-14} mm.

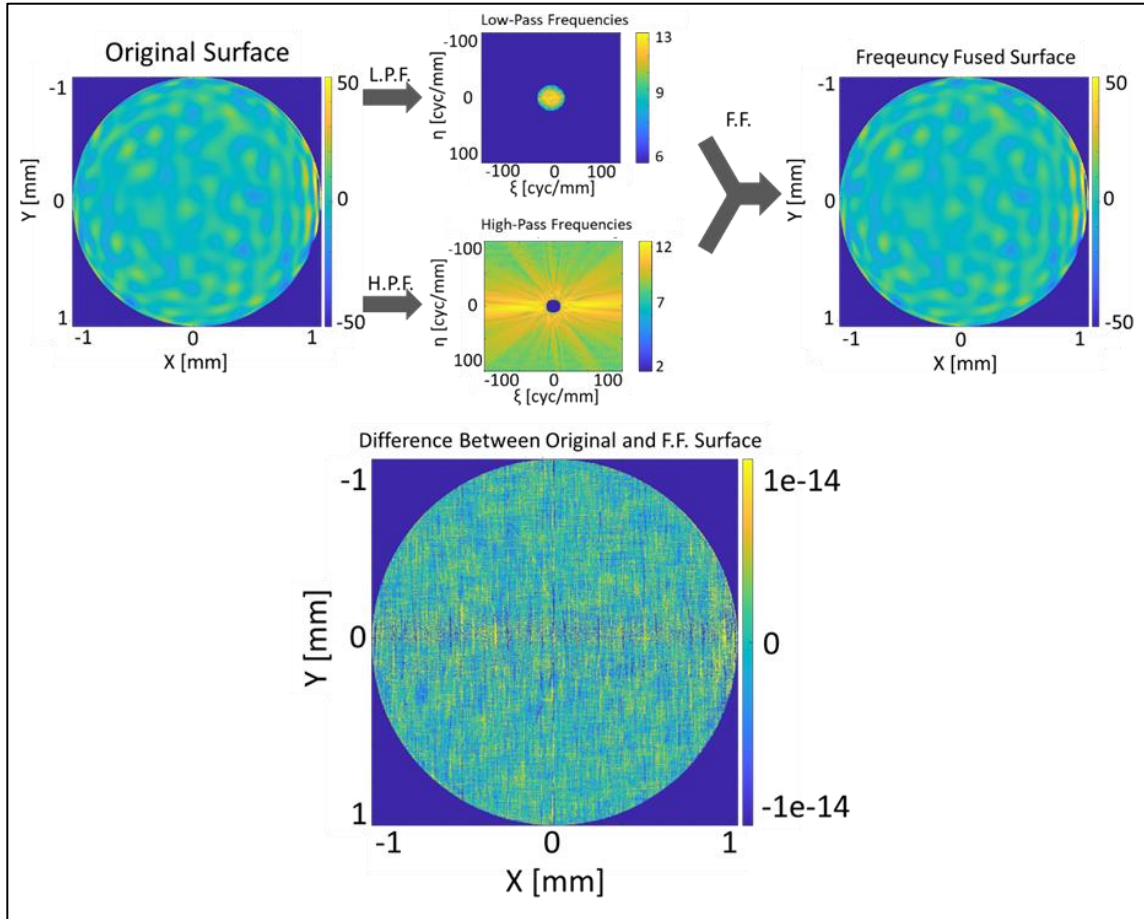


Figure 21. Results of applying low and high-pass filters to the randomly generated synthetic data set, frequency fusing the filters, and comparing the merged surface to the original.

Chapter 5. Conclusions and Future Work

All optical metrology testing shares a common tradeoff between FoV and resolution. Having a high resolution over a large field of view is ultimately desirable, however is intrinsically limited due to this tradeoff. Sub-aperture stitching attempts to overcome this limitation by stitching together many high-resolution sub-apertures, however, it struggles in achieving high accuracy in the low-order surface structure. The frequency fusion process introduced here compensates for unreliability in the low-order surface shape information from the stitched interferometric map by using low-order deflectometry data as a reliable framework to place accurate high-order interferometric data on to.

By merging together deflectometry and WLI data through use of frequency fusion masks, high accuracy in both the high and low-order surface shape is achieved. The size and weighting of the masks used during the frequency fusion process can be adjusted to match the reliability of the frequencies being combined over, making it a robust and highly flexible tool. Ideally, the window in which the spatial frequency merging is done over would have 100% trustable information from both data sets in order to produce a smooth transition between the low and high-order frequency surface structure. However, complete confidence between data sets is unlikely, so determining how the reliability in each data set changes over the merging window is necessary to properly fuse the data together. In future studies this trend in reliability could be determined by measuring a well characterized surface structure and comparing the measurements made by the different metrology techniques to the expected results.

Chapter 6. References

- [1] D. Mills and H. Padmore, “X-ray Optics for BES Light Source Facilities,” p. 150.
- [2] K. Okada, “Measurement of large plane surface shapes by connecting small-aperture interferograms,” *Opt. Eng.*, vol. 33, no. 2, p. 608, Feb. 1994, doi: [10.1117/12.152248](https://doi.org/10.1117/12.152248).
- [3] M. C. Knauer, J. Kaminski, and G. Hausler, “Phase measuring deflectometry: a new approach to measure specular free-form surfaces,” Strasbourg, France, Sep. 2004, p. 366. doi: [10.1117/12.545704](https://doi.org/10.1117/12.545704).
- [4] R. Ritter and R. Hahn, “Contribution to analysis of the reflection grating method,” *Optics and Lasers in Engineering*, vol. 4, no. 1, pp. 13–24, Jan. 1983, doi: [10.1016/0143-8166\(83\)90003-9](https://doi.org/10.1016/0143-8166(83)90003-9).
- [5] H. Quach *et al.*, “Surface Measurement of a Large Inflatable Reflector in Cryogenic Vacuum,” *Photonics*, vol. 9, no. 1, p. 1, Dec. 2021, doi: [10.3390/photonics9010001](https://doi.org/10.3390/photonics9010001).
- [6] J. M. Kam, "Differential Phase Measuring Deflectometry for High-Sag Freeform Optics." Order No. 27670957, The University of Arizona, Ann Arbor, 2019.
- [7] C. Faber, E. Olesch, R. Krobot, and G. Häusler, “Deflectometry challenges interferometry: the competition gets tougher!,” San Diego, California, USA, Sep. 2012, p. 84930R. doi: [10.1117/12.957465](https://doi.org/10.1117/12.957465).
- [8] James C. Wyant, “White light interferometry,” Jul. 2002, vol. 4737. doi: [10.1117/12.474947](https://doi.org/10.1117/12.474947).
- [9] R. Huang, “HIGH PRECISION OPTICAL SURFACE METROLOGY USING DEFLECTOMETRY,” p. 173.

[10] E. P. Goodwin and J. C. Wyant, *Field Guide to Interferometric Optical Testing*. SPIE, 2006. doi: [10.1117/3.702897](https://doi.org/10.1117/3.702897)

